Stability and Population Oscillations in a Spin–Orbit Coupled Bose–Einstein Condensate

Q. Zhu[a] and C. Kong[b,*]

[a] *College of Science, Hunan University of Technology, Zhuzhou 412007, China*
[b] *School of Physics and Electronic-Electrical Engineering, Xiangnan University, Chenzhou 423000, China*

Received: 14.12.2024 & Accepted: 10.03.2025

Doi: 10.12693/APhysPolA.147.309 *e-mail: superkong@xnu.edu.cn

In this paper, we have investigated the stability and population oscillations in a spin–orbit coupled Bose–Einstein condensate. For the time-independent system parameters, the stability of the steady-state solutions was analyzed with the linear stability theorem. For the asymmetric case, we demonstrated that a larger relative energy can enhance macroscopic quantum self-trapping. A larger relative energy or a stronger population transfer strength can assist or suppress the tunneling rate, depending on the initial population. Finally, the chaotic parameter regions and the chaotic atomic tunneling between two periodically driven Bose–Einstein condensates have been investigated. The results reveal that chaos can notably enhance the tunneling rate. The results could be significant in the quantum transport of the spin–orbit coupled cold-atom system.

topics: Bose–Einstein condensate (BEC), spin–orbit (SO) coupling, population oscillations, stability

1. Introduction

The experimental generation of Bose–Einstein condensation (BEC) [1, 2] has provided us with a valuable platform for exploring numerous core phenomena in atomic physics, condensed matter physics, and quantum optics. Spin–orbit coupling (SOC) — a concept that describes the subtle interaction between spin and momentum of quantum particles — plays a crucial role in many condensation phenomena, such as the spin Hall effect [3, 4] and topological insulators [5]. In addition, it has immeasurable value in revealing the electronic properties of materials and promoting the development of spintronics devices [5]. Of particular note, in 2011, Spielman's research team successfully achieved SOC in ^{87}Rb BEC system [6]. This milestone achievement greatly broadens the boundaries and perspectives of ultracold atoms as a quantum simulation platform [7–18].

It is noteworthy that BEC, being a many-body system, operates under the Gross–Pitaevskii (GP) mean-field equation, which serves as a crucial cornerstone for investigating macroscopic quantum (or semi-classical) chaos. The existence of chaos in BEC has been established and its chaotic attributes have been extensively examined in numerous studies [19–27]. Researchers are committed to exploring the chaos phenomena within BEC systems and understanding its implications on the system dynamics. Notably, the investigation of chaos in transportation of atoms holds considerable practical application significance. In [28], the authors studied the impact of chaotic dynamics on the atomic tunneling between two BECs that are weakly coupled and driven by bichromatic periodic fields, advancing the perspective that chaos can substantially enhance the atomic tunneling rates. Additionally, in [29], the chaotic transport of matter wave solitons in a biperiodically driven optical superlattice was studied, discovering that high chaoticity can substitute for higher disorder in the Anderson localization. Spin–orbit (SO) coupled BEC constitutes an even more intricate nonlinear system, capable of exhibiting chaotic behavior under specific parametric conditions [30–33]. The emergence of chaos can potentially destabilize the system and culminate in its collapse. Consequently, the exploration of the possibility of controlling the behavior of chaos within a SO coupled BEC systems is imperative and holds a significant standing in the realm of chaos applications.

In this paper, we have investigated the stability of the steady-states and population oscillations excited by time-independent system parameters in a SO coupled BEC. Meanwhile, the chaotic parameter regions and atomic tunneling between two periodically driven BEC have been investigated. The whole presentation is structured as follows. In Sect. 2, we introduce a model based on a SO coupled BEC in a single well and use the linear stability theorem to study the stability of the steady-states. In Sect. 3, for the asymmetric case, we demonstrate that a larger relative energy or a stronger population transfer strength can assist or suppress the tunneling rate, depending on the initial population. In Sect. 4, we numerically show that chaos can significantly enhance the tunneling rate between two periodically driven BEC. Finally, Sect. 5 concludes the paper.

2. Stability analysis of the steady-state solutions

Consider a SO coupled BEC confined in a single-well potential. The system is governed by the nonlinear Schrödinger equations, as detailed in [33–36],

$$\mathrm{i}\frac{\partial \Psi_j}{\partial t} = \Big[-\frac{1}{2}\frac{\partial^2}{\partial x^2} + V(x) + (-1)^j \Gamma\Big]\Psi_j - \Big(\mathrm{i}\gamma\frac{\partial}{\partial x} - \widetilde{\delta}\Big)\Psi_{3-j} + \Big(g|\Psi_j|^2 + g_{12}|\Psi_{3-j}|^2\Big)\Psi_j, \tag{1}$$

for $j = 1, 2$. Here, the units of x, t, and probability density $|\Psi_j|^2$ are $a_\perp$, $\omega_\perp^{-1}$, and $a_\perp^{-1}$, respectively, where $a_\perp = \sqrt{\hbar/m\omega_\perp}$ represents the harmonic oscillator length of the transverse trap, following the conventions in [33]. The parameters $\widetilde{\delta}$, γ, and Γ denote the dimensionless detuning strength, the SO, and Rabi coupled strengths, respectively. The interaction strengths are given by g and g_{12}. We adopt the separable ansatz $\Psi_j(x,t) = \psi_j(t)\varphi_j(x) (j = 1, 2)$ for $j = 1, 2$, with $\varphi_j(x)$ satisfying $\int \mathrm{d}x\ \varphi_j^2(x) = 1$ and $\int \mathrm{d}x\ \varphi_i(x)\varphi_j(x) < 1$ for $i \neq j$. Substituting $\Psi_j(x,t)$ into (1) and integrating spatially, we derive the corresponding nonlinear equations

$$\mathrm{i}\frac{\partial \psi_1(t)}{\partial t} = \big(E_1 - \Gamma + U_1|\psi_1|^2 + U_{12}|\psi_2|^2\big)\psi_1 + (\kappa - \mathrm{i}\widetilde{\gamma})\psi_2, \tag{2}$$

$$\mathrm{i}\frac{\partial \psi_2(t)}{\partial t} = \big(E_2 + \Gamma + U_2|\psi_2|^2 + U_{12}|\psi_1|^2\big)\psi_2 + (\kappa + \mathrm{i}\widetilde{\gamma})\psi_1. \tag{3}$$

Here, $E_j = \int \mathrm{d}x\ \varphi_j(x)\big[-\frac{1}{2}\frac{\partial^2}{\partial x^2} + V(x)\big]\varphi_j(x)$, $U_j = g\int \mathrm{d}x\ \varphi_j^4(x)$, and $U_{12} = g_{12}\int \mathrm{d}x\ \varphi_1^2(x)\varphi_2^2(x)$ denote the zero-point energies, mean-field intra- and inter-species interaction, respectively. The parameters $\kappa = \widetilde{\delta}\int \mathrm{d}x\ \varphi_1(x)\varphi_2(x)$ and $\widetilde{\gamma} = \gamma\int \mathrm{d}x\ \varphi_1(x)\frac{\partial}{\partial x}\varphi_2(x)$ describe the population transfer and the SOC term, respectively. We consider $\psi_j(t) = \sqrt{N_j(t)}\exp[\mathrm{i}\theta_j(t)]$ with $N_j(t) = |\psi_j(t)|^2$ and $\theta_j(t)$ being the numbers and phases of the BEC components. We define $z(t) = N_2(t) - N_1(t)$ and $\phi(t) = \theta_2(t) - \theta_1(t)$ being, respectively, the relative population imbalance and phase, and obtain the coupled equations

$$\dot{z}(t) = -2\sqrt{1-z^2}\Big[\kappa\sin(\phi) - \widetilde{\gamma}\cos(\phi)\Big], \tag{4}$$

$$\dot{\phi}(t) = \Delta E + \Lambda z + \frac{2z}{\sqrt{1-z^2}}\Big[\widetilde{\gamma}\sin(\phi) + \kappa\cos(\phi)\Big], \tag{5}$$

where $\Lambda = \frac{U_1+U_2}{2} - U_{12}$ is the atomic scattering length and $\Delta E = E_1 - E_2 - 2\Gamma + \frac{U_1-U_2}{2}$ denotes the energy difference. The conserved Hamiltonian can be obtained as

$$H = -2\sqrt{1-z^2}\Big[\widetilde{\gamma}\sin(\phi) + \kappa\cos(\phi)\Big] + \Delta E\, z + \frac{\Lambda}{2}z^2. \tag{6}$$

In this section, we use the linear stability theorem to study the stability of steady-state in the symmetric case ($\Delta E = 0$). When (4) and (5) are equal to 0, we can obtain the steady-state solution of the system. With non-zero relative energy, it's complex. Hence, we simplify by considering $\Delta E = 0$. Therefore, (4) and (5) can be simplified into the following form

$$\dot{z}(t) = f_1(z,\theta) = -2\sqrt{1-z^2}\Big[\kappa\sin(\phi) - \widetilde{\gamma}\cos(\phi)\Big], \tag{7}$$

$$\dot{\phi}(t) = f_2(z,\theta) = \Lambda z + \frac{2z}{\sqrt{1-z^2}}\Big[\widetilde{\gamma}\sin(\phi) + \kappa\cos(\phi)\Big]. \tag{8}$$

Setting $\dot{z} = 0$ and $\dot{\phi} = 0$, we can obtain the steady-state solutions of (7) and (8), i.e.,

- for $H = -2\sqrt{\kappa^2+\widetilde{\gamma}^2}$,

$$z_1 = 0, \quad \phi_1 = -\arccos\Big(-\kappa/\sqrt{\kappa^2+\widetilde{\gamma}^2}\Big), \tag{9}$$

- for $H = \frac{\Lambda}{2} + \frac{2(\kappa^2+\widetilde{\gamma}^2)}{\Lambda}$,

$$z_{2,3} = \pm\frac{\sqrt{\Lambda^2 - 4\kappa^2 - 4\widetilde{\gamma}^2}}{\Lambda}, \quad \phi_{2,3} = -\arccos\Big(-\kappa/\sqrt{\kappa^2+\widetilde{\gamma}^2}\Big). \tag{10}$$

According to the linear stability theorem, we seek perturbed solutions that are near steady-state solutions,

$$z(t) = z_i(t) + \epsilon_1(t), \qquad \phi(t) = \phi_i(t) + \epsilon_2(t), \tag{11}$$

where $z_i(t)$, $\phi_i(t)$ (for $i = 1, 2, 3$) represent steady-state solutions, $\epsilon_1(t)$ and $\epsilon_2(t)$ are the first-order perturbed corrections. Substituting the above expressions into (7) and (8), we can obtain linear equations as

$$\dot{\epsilon}_1 = a_{11}\epsilon_1 + a_{12}\epsilon_2, \qquad \dot{\epsilon}_2 = a_{21}\epsilon_1 + a_{22}\epsilon_2. \tag{12}$$

Here, $a_{ij} = (\frac{\partial f_i}{\partial x_i})_0$, where x_i represents the state variable, and the subscript "0" represents the value at the fixed point. Now we discuss the stabilities of the three steady-states of (9) and (10).

2.1. Stability of the steady-state (z_1, ϕ_1)

For the steady-state (z_1, ϕ_1), we can easily calculate $a_{11} = 0$, $a_{22} = 0$, $a_{12} = 2\sqrt{\kappa^2+\widetilde{\gamma}^2}$, and $a_{21} = \Lambda - 2\sqrt{\kappa^2+\widetilde{\gamma}^2}$. The coefficient matrix of the linearized equation (12) becomes

$$\mathbb{A} = \begin{bmatrix} 0 & 2\sqrt{\kappa^2+\widetilde{\gamma}^2} \\ \Lambda - 2\sqrt{\kappa^2+\widetilde{\gamma}^2} & 0 \end{bmatrix} \tag{13}$$

such that the characteristic equation reads

$$\det(\mathbb{A} - \lambda\mathbb{I}) = \begin{bmatrix} -\lambda & 2\sqrt{\kappa^2+\widetilde{\gamma}^2} \\ \Lambda - 2\sqrt{\kappa^2+\widetilde{\gamma}^2} & -\lambda \end{bmatrix} = 0, \tag{14}$$

which implies that $\lambda^2 - 2\sqrt{\kappa^2+\widetilde{\gamma}^2}\,(\Lambda - 2\sqrt{\kappa^2+\widetilde{\gamma}^2}) = 0$. This gives the two eigenvalues

$$\lambda_1 = \sqrt{2\sqrt{\kappa^2+\widetilde{\gamma}^2}(\Lambda - 2\sqrt{\kappa^2+\widetilde{\gamma}^2})}, \tag{15}$$

$$\lambda_2 = -\sqrt{2\sqrt{\kappa^2+\widetilde{\gamma}^2}(\Lambda - 2\sqrt{\kappa^2+\widetilde{\gamma}^2})}. \tag{16}$$

According to the forms of the eigenvalues, there exist two cases for stabilities:

(i) When $\Lambda > 2\sqrt{\kappa^2+\widetilde{\gamma}^2}$, the two eigenvalues are positive and negative real number, respectively. This means that ε_1 and ε_2 will tend to infinity with increasing time, and the steady-state solutions (z_1, ϕ_1) are unstable.

(ii) When $\Lambda \leq 2\sqrt{\kappa^2+\widetilde{\gamma}^2}$, the two eigenvalues are both pure imaginary numbers. In this case, the stability of the steady state solutions (z_1, ϕ_1) corresponds to a critical case, and the dynamical bifurcations between the unstable and stable steady-states will appear.

2.2. Stability of the steady-states $(z_{2,3}, \phi_{2,3})$

For the steady-state $(z_{2,3}, \phi_{2,3})$, we can easily calculate $a_{11} = 0$, $a_{22} = 0$, $a_{12} = 4(\kappa^2+\widetilde{\gamma}^2)/\Lambda$, and $a_{21} = \Lambda[1 - \Lambda^2/(4(\kappa^2+\widetilde{\gamma}^2))]$. The coefficient matrix of the linearized equation (12) becomes

$$\mathbb{A} = \begin{bmatrix} 0 & \frac{4(\kappa^2+\widetilde{\gamma}^2)}{\Lambda} \\ \Lambda(1 - \frac{\Lambda^2}{4(\kappa^2+\widetilde{\gamma}^2)}) & 0 \end{bmatrix}, \tag{17}$$

such that the characteristic equation reads

$$\det(\mathbb{A} - \lambda\mathbb{I}) = \begin{bmatrix} -\lambda & \frac{4(\kappa^2+\widetilde{\gamma}^2)}{\Lambda} \\ \Lambda(1 - \frac{\Lambda^2}{4(\kappa^2+\widetilde{\gamma}^2)}) & -\lambda \end{bmatrix} = 0, \tag{18}$$

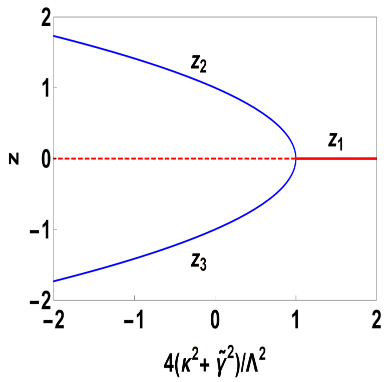

Fig. 1. Plot of the tuning-fork bifurcation obtained from (9). The bifurcation point reads $4(\kappa^2+\widetilde{\gamma}^2)/\Lambda^2 = 1$. The solution $z_1 = 0$ plotted by the solid curve is critically stable, while the one depicted by the dashed line denotes the unstable steady-state. The solutions z_2 and z_3 describe the stable states.

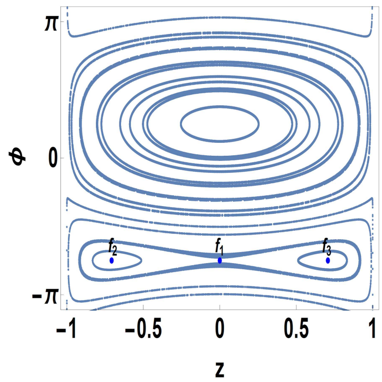

Fig. 2. Plot of the classical phase space trajectory obtained from (4) and (5) with parameters $\kappa = 0.5$, $\widetilde{\gamma} = 0.5$, and $\Lambda = 2$.

which gives the two eigenvalues as

$$\lambda_1 = 2\sqrt{(\kappa^2+\widetilde{\gamma}^2)\left(1 - \frac{\Lambda^2}{4(\kappa^2+\widetilde{\gamma}^2)}\right)}, \tag{19}$$

$$\lambda_2 = -2\sqrt{(\kappa^2+\widetilde{\gamma}^2)\left(1 - \frac{\Lambda^2}{4(\kappa^2+\widetilde{\gamma}^2)}\right)}. \tag{20}$$

In (10), the population $z_{2,3}$ being a real quantity means $\Lambda^2 > 4(\kappa^2+\widetilde{\gamma}^2)$. Therefore, the two eigenvalues are both pure imaginary numbers, which means that the steady-state solutions $(z_{2,3},\ \phi_{2,3})$ are stable. In this case, the stability of the steady-state solutions $(z_{2,3},\ \phi_{2,3})$ corresponds to a critical case, and dynamical bifurcations between unstable and stable steady-states will appear.

From (9) we plot the bifurcation configuration as in Fig. 1. The bifurcation point reads $4(\kappa^2+\widetilde{\gamma}^2)/\Lambda^2 = 1$. In the parameter region $4(\kappa^2+\widetilde{\gamma}^2)/\Lambda^2 > 1$, the system is in the

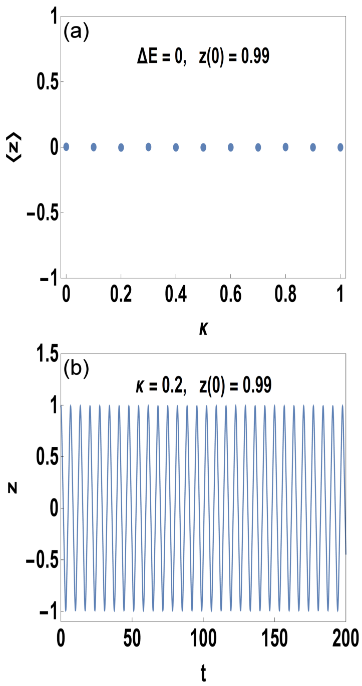

Fig. 3. (a) The average population as a function of the population transfer κ between two BEC states with initial condition $z(0) = 0.99$ and $\phi(0) = \pi/4$ and parameters $\Delta E = 0$, $\Lambda = 2$, $\widetilde{\gamma} = 0.5$. (b) The corresponding time evolutions of population $z(t)$ for the labeled parameter.

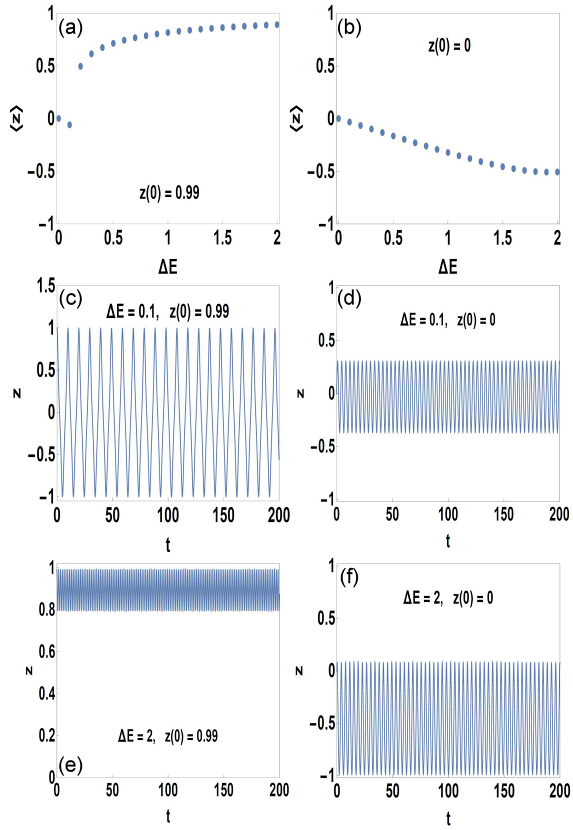

Fig. 4. The average population as a function of the relative energy ΔE with the initial condition (a) $z(0) = 0.99$, (b) $z(0) = 0$ and $\phi(0) = \pi/4$ and the parameters $\kappa = 0.1$, $\widetilde{\gamma} = 0.5$, and $\Lambda = 2$. (c–f) The corresponding time evolutions of the population $z(t)$ for labeled initial states and parameters.

critically stable steady-state (z_1, ϕ_1). In the region $4(\kappa^2+\widetilde{\gamma}^2)/\Lambda^2 < 1$, (z_1, ϕ_1) is unstable, and the two new steady-state solutions $(z_{2,3}, \phi_{2,3})$ are critically stable. In Fig. 2, we give the classical phase space plot for the symmetric case with parameters $\kappa = 0.5$, $\widetilde{\gamma} = 0.5$ and $\Lambda = 2$, where the phase space consists of closed rings, indicating periodic or quasi-periodic trajectories. With these parameters in the diagram, f_2 and f_3 represent the stable fixed points (centers) $(z_2, \phi_2) = (-0.71, -2.36)$ and $(z_3, \phi_3) = (0.71, -2.36)$, respectively, while f_1 represents the unstable fixed point (saddle point) $(z_1, \phi_1) = (0, -2.36)$.

3. Population oscillations excited by time-independent system parameters

We now investigate the dynamic behavior governed by (4) and (5) with time-independent system parameters. Starting from this set of equations, we analyze the effects of the parameters on the population oscillations with a numerical method. Here, we use the average population imbalance $\langle z \rangle = \frac{1}{400}\int_0^{400} \mathrm{d}t\, z(t)$ to display the distinct differences in the atomic population oscillations. The nonzero average value denotes the appearance of macroscopic quantum self-trapping (MQST).

In Fig. 3a, we plot the average population imbalance $\langle z \rangle$ as a function of the population transfer κ between two BEC states with initial condition $z(0) = 0.99$ and $\phi(0) = \pi/4$ and parameters $\Delta E = 0$, $\Lambda = 2$, $\widetilde{\gamma} = 0.5$. The values of the average population balance are zero for the symmetric case $\Delta E = 0$, so the corresponding MQST does not appear. In Fig. 3b, we plot the atomic population oscillations for the population transfer $\kappa = 0.2$, where periodical features are observed.

Next, we investigate the population oscillations in the asymmetric case ($\Delta E \neq 0$). The average population as a function of the relative energy ΔE are plotted for $z(0) = 0.99$ in Fig. 4a and for $z(0) = 0$ in Fig. 4b, with $\phi(0) = \pi/4$ and parameters $\kappa = 0.1$, $\widetilde{\gamma} = 0.5$, and $\Lambda = 2$. When the majority of the atoms are initially concentrated in one of the components $z(0) = 0.99$, the values of the average population balance increase with increasing relative energy, as shown in Fig. 4a, which means that MQST is enhanced. Comparing Fig. 4c and Fig. 4e, as the relative energy increases from 0.1 to 2, the amplitude of the atomic population decreases, indicating that higher relative energy diminishes

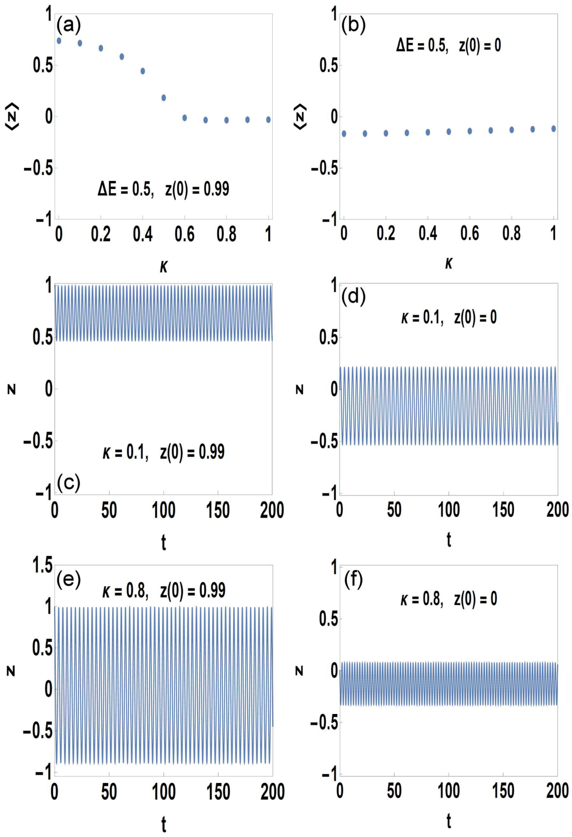

Fig. 5. The average population as a function of the population transfer κ between two BEC states with the initial condition (a) $z(0) = 0.99$, (b) $z(0) = 0$ and $\phi(0) = \pi/4$ and the parameters $\Delta E = 0.5$, $\widetilde{\gamma} = 0.5$. (c–f) The corresponding time evolutions of the population $z(t)$ for labeled initial states and parameters.

population transfer between atoms. When the atoms are initially evenly distributed between the two components $z(0) = 0$, the absolute values of the average population balance increase with increasing relative energy, as shown in Fig. 4b. This observation indicates that the MQST effect is enhanced. Comparing Fig. 4d and Fig. 4f, we note that when the relative energy increases from 0.1 to 2, the amplitude of the atomic population balance increases, suggesting that a larger relative energy promotes or facilitates population transfer between atoms.

The average population as a function of the population transfer κ is plotted in Fig. 5a for $z(0) = 0.99$ and in Fig. 5b for $z(0) = 0$. In Fig. 5a, the values of the average population balance decrease with the increase in the population transfer κ, which means that MQST is suppressed. For the same initial state $z(0) = 0.99$ and $\phi(0) = \pi/4$, regular behavior with periodic population oscillations is shown in Fig. 5c for $\kappa = 0.1$ and in Fig. 5e for $\kappa = 0.8$. Clearly, the results imply that the stronger population transfer can enhance the transfer of atoms between the two states. In Fig. 5b, for a fixed initial population $z(0) = 0$, the absolute values of the average population balance decrease with the increase in the population transfer κ, which means that MQST is suppressed. The periodic collapses appear in Fig. 5d and 5f for the labeled parameters. The amplitude of $z(t)$ in Fig. 5d is greater than that in Fig. 5f. This illustrates that the stronger population transfer can reduce the transfer of atoms notably.

4. Parametric excitation of chaotic population oscillations

If a time-periodical trap potential is considered, the trap asymmetry $\Delta E(t)$ and the tunneling dynamics $\kappa(t)$ are time-dependent. Experimentally, due to the small oscillation of the laser position and its intensity, the parameters $\Delta E(t)$ and $\kappa(t)$ can be written as [37]

$$\Delta E(t) = \Delta E_0 - \Delta E_1 \sin(\omega t),$$
$$\kappa(t) = -\kappa_1 \sin(2\omega t). \tag{21}$$

Then we yield the perturbed Duffing equation of $z(t)$

$$\ddot{z} = \frac{\partial \dot{z}}{\partial z}\dot{z} + \frac{\partial \dot{z}}{\partial \phi}\dot{\phi} + \frac{\partial \dot{z}}{\partial k}\dot{k} = \left(\Lambda H - 4\kappa(t)^2 - 4\widetilde{\gamma}^2\right) z - \frac{\Lambda^2}{2} z^3 + F(t), \tag{22}$$

$$F(t) = \left(H - \Delta E(t)\, z - \frac{3\Lambda}{2}\, z^2 - \frac{\widetilde{\gamma}\, z\, \dot{\kappa}(t)}{\kappa^2(t) + \widetilde{\gamma}^2}\right) \Delta E(t) + \frac{2H\widetilde{\gamma} - 2\kappa(t)\, \dot{z} - \widetilde{\gamma}\Lambda\, z^2}{2(\kappa^2(t) + \widetilde{\gamma}^2)} \dot{\kappa}(t). \tag{23}$$

In this section, we will study the chaotic motion of the system. Firstly, we consider $|\kappa_1| \ll 1$ and $|\Delta E_{0,1}| \ll 1$ and seek the perturbed solution of (22). The population z and Hamiltonian H can be expressed as

$$z = z_0 + z_1, \qquad |z_0| \gg |z_1| \sim |\kappa_1|, |\Delta E_{1,0}|, \tag{24}$$

$$H = H_0 + H_1, \qquad |H_0| \gg |H_1| \sim |\kappa_1|, |\Delta E_{1,0}|. \tag{25}$$

where z_1 and H_1 are the first-order corrections. Substituting them into (22) will produce the zero-order equations

$$\ddot{z}_0 = \left(\Lambda H_0 - 4\widetilde{\gamma}^2\right) z_0 - \frac{\Lambda^2}{2}\, z_0^3, \tag{26}$$

$$H_0 = -2\sqrt{1 - z_0^2}\, \widetilde{\gamma}\, \sin(\phi) + \frac{\Lambda}{2}\, z_0^2, \tag{27}$$

and the first-order equations

$$\ddot{z}_1 = \left(\Lambda H_0 - 4\widetilde{\gamma}^2\right) z_1 - \frac{3\Lambda^2}{2}\, z_0^2 z_1 + \epsilon, \tag{28}$$

$$H_1 = \int \mathrm{d}t \left[-\Delta E_1 \omega \cos(\omega t) z_0 + \frac{2\kappa_1 \omega}{\widetilde{\gamma}} \cos(2\omega t) \dot{z}_0 \right], \tag{29}$$

$$\epsilon = \Delta E\Big(H_0 - \frac{3\Lambda}{2} z_0^2\Big) + \Lambda H_1 z_0 + \frac{2\kappa_1 \omega}{\widetilde{\gamma}} \sin(2\omega t) \times\Big(H_0 - \frac{\Lambda}{2} z_0^2\Big), \tag{30}$$

where ϵ and H_0 are the perturbation function and a conserved constant Hamiltonian, respectively [25, 38, 39]. The homoclinic solution of the zero-order equation (26) is as follow

$$z_0(t) = \frac{2\sqrt{\widetilde{H}}}{\Lambda} \mathrm{sech}(\xi), \qquad \xi = \sqrt{\widetilde{H}}\, t + c,$$
$$\widetilde{H} = \left(\Lambda H_0 - 4\widetilde{\gamma}^2\right),$$
$$c = \mathrm{Ar\,sech}\left(\frac{\Lambda z_0(t_0)}{2\sqrt{\widetilde{H}}}\right) - \sqrt{\widetilde{H}}\, t_0, \tag{31}$$

where the constant c depends on the initial population $z(t_0)$ and the system parameters with constant $\widetilde{H} > 0$. We take the initial time $t_0 = 0$ and obtain linearly independent solutions of the first-order equation (28) with $\epsilon = 0$

$$h = \frac{\mathrm{d}z_0}{\mathrm{d}t} = -\frac{2\widetilde{H}}{\Lambda} \mathrm{sech}(\xi) \tanh(\xi), \tag{32}$$

$$f = h \int \mathrm{d}t\ h^{-2} = \frac{\Lambda}{8\widetilde{H}^{3/2}} \mathrm{sech}(\xi) \tanh(\xi) \times \Big[4 \coth(\xi) - \sinh(2\xi) - 6\xi\Big]. \tag{33}$$

Then we have the general solution of the first-order equation (27) [40–42]

$$z_1 = f \int_A^x \mathrm{d}x\ (h\,\epsilon) - h \int_B^x \mathrm{d}x\ (f\,\epsilon). \tag{34}$$

Here, the constants A and B are determined by the initial conditions. Obviously, when time $t \to \infty$, we have $f \to \infty$ corresponding to the unbounded general solution (34). The necessary-sufficient condition for the bounded solution (34) is [25, 40–42]

$$I_{\pm} = \lim_{t \to \pm\infty} \int_A^x \mathrm{d}t\ h\epsilon = 0, \tag{35}$$

which gives the Melnikov chaos criterion [43]

$$M(c) = I_+ - I_- = \int_{-\infty}^{+\infty} \mathrm{d}t\ (h\epsilon) = D_1 \cos\left(\frac{c\,\omega}{\sqrt{\widetilde{H}}}\right) + \kappa_1 D_2 \sin\left(\frac{2c\,\omega}{\sqrt{\widetilde{H}}}\right) = 0, \tag{36}$$

$$D_1 = -\frac{2\pi \Delta E_1 \omega \left(\widetilde{H} - \Lambda H_0 + \omega^2\right) \mathrm{sech}\left(\frac{\pi\omega}{2\sqrt{\widetilde{H}}}\right)}{\Lambda^2}, \tag{37}$$

$$D_2 = -\frac{8\pi\, \omega^2 \left(\widetilde{H} - 3\Lambda H_0 + 4\omega^2\right) \mathrm{sech}\left(\frac{\pi\omega}{\sqrt{\widetilde{H}}}\right)}{3\Lambda^2 \widetilde{\gamma}}, \tag{38}$$

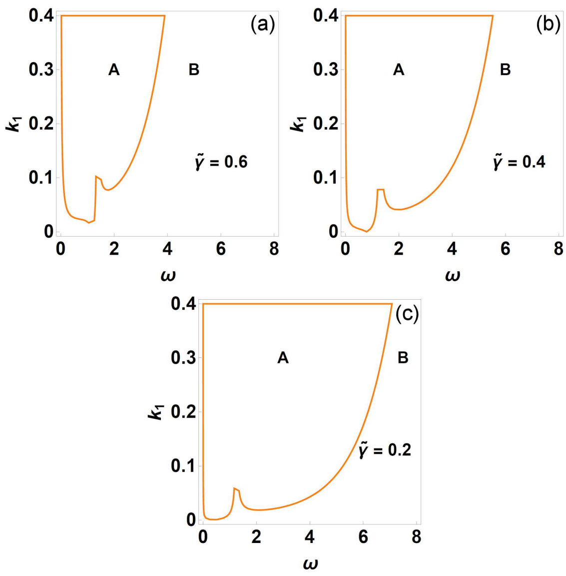

Fig. 6. Boundaries between regular and chaotic regions for different SOC strengths: (a) $\widetilde{\gamma} = 0.6$, (b) $\widetilde{\gamma} = 0.4$, and (c) $\widetilde{\gamma} = 0.2$. Areas marked by A are chaotic regions and areas marked by B are regular regions. The other parameters are taken as $\Lambda = 3$, $\Delta E_1 = 0.2$, and $H_0 = 1$.

indicating the appearance of Melinokov chaos. To give the boundaries between different regions, we can obtain from (36) $\sin(c\omega/\sqrt{\widetilde{H}}) = -D_1/(2\kappa_1 D_2)$. Due to $|\sin(c\omega/\sqrt{\widetilde{H}})| \le 1$, we obtain the chaotic region in the parameter space

$$\kappa_1 \ge \left| \frac{D_1}{2D_2} \right|. \tag{39}$$

In Fig. 6, from (39) we plot the chaos-dependent parameter regions on the plane (κ_1, ω) for different SOC strengths: (a) $\widetilde{\gamma} = 0.6$, (b) $\widetilde{\gamma} = 0.4$, and (c) $\widetilde{\gamma} = 0.2$. The other parameters are taken as $\Lambda = 3$, $\Delta E_1 = 0.2$, and $H_0 = 1$. The areas marked by A are chaotic regions and the areas marked by B are regular regions. Obviously, the value of the SOC strength is inversely proportional to the size of the chaotic region.

Next, in order to study the parametric excitation of chaotic atomic population oscillations, we plot the average population as a function of the driving frequency ω with parameters $\kappa_1 = 0.2$, $\widetilde{\gamma} = 0.6$, $\Delta E_0 = 0.2$, $\Delta E_1 = 0.2$, $\Lambda = 3$ and initial conditions $z(0) = 0.99$, $\phi(0) = \pi/4$. In Fig. 7a, for $\kappa_1 = 0.2$, as we vary the driving frequency and make the system pass through the chaotic region and regular ones, smaller values of the average atomic population appear for the parameters located in the chaotic region of Fig. 6a, denoting the suppressed MQST. Chaotic behavior in Fig. 7b with irregular population oscillations appears for the driving frequency $\omega = 1.5$ located in the chaotic region of Fig. 6a, and obvious chaos-enhanced population transfer can also be identified by the greater amplitudes of population

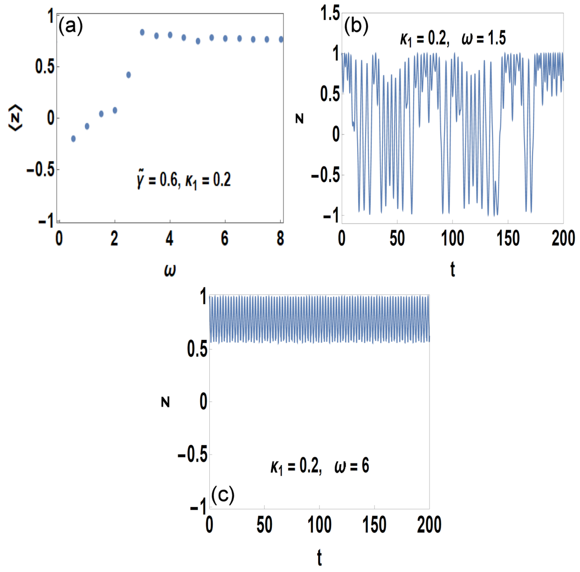

Fig. 7. (a) The average population as a function of the driving frequency ω with parameters $\kappa_1 = 0.2$, $\widetilde{\gamma} = 0.6$, $\Delta E_0 = 0.2$, $\Delta E_1 = 0.2$, $\Lambda = 3$ and initial conditions $z(0) = 0.99$, $\phi(0) = \pi/4$. (b–c) The corresponding time evolutions of the population $z(t)$ for labeled parameters. The other parameters are the same as those in Fig. 5a.

balance. The regular behavior with periodic population oscillation is shown in Fig. 7c for the driving frequency $\omega = 6$ located in the regular parameter region. Obviously, the non-zero time-averaged value of the population denotes the presence of MQST. With these numerical results, we demonstrate that the atomic tunneling is enhanced notably owing to the presence of chaos.

5. Conclusions

In this paper, we have investigated the stability and population oscillations excited by the system parameters in a SO coupled BEC. Firstly, the stabilities of the steady state solutions were analyzed with the linear stability theorem and a typical tuning-fork bifurcation of the steady-state relative population was found, which is shown in Fig. 1. Then, we studied the population oscillations excited by time-independent system parameters. We numerically found that when $\Delta E = 0$ and the initial conditions $z(0) = 0.99$ and $\phi(0) = \pi/4$ are selected, MQST does not appear. For the asymmetric case, we observe that the amplitude of $z(t)$ shows an energy-dependent behavior that varies with initial conditions: (i) When atoms are initially evenly distributed ($z(0) = 0$), the amplitude increases with energy, suggesting enhanced inter-component atom transfer; (ii) Conversely, when most atoms initially occupy one component ($z(0) = 0.99$), the amplitude decreases with increasing energy, indicating suppressed transfer. In addition, when the initial condition $z(0) = 0.99$ is selected, the stronger population transfer can enhance the transfer of atoms between the two states. While for the initial condition $z(0) = 0$, the stronger population transfer can notably reduce the transfer of atoms. Finally, we analytically obtained the chaotic perturbed solution and numerically plot the chaotic parameter regions by using the Melnikov chaos criterion. We found that stronger SOC strength can reduce the size of the chaotic regions. The effects of chaotic dynamics on MQST have been studied. It is revealed that chaos can significantly enhance the tunneling rate. The results could be significant in the quantum transport of the SO coupled cold-atom system.

It is also known that the parametric excitation of chaotic population oscillations via square-wave driving in the dissipative regime was reported in Section IV in [44], while our work is centered on chaotic population oscillations in the nondissipative regime. The key difference with the mentioned paper is that we obtained chaotic parameter regions and chaotic atomic tunneling between two periodically driven BEC, where the trap asymmetry $\Delta E(t)$ and the tunneling dynamics $\kappa(t)$ are time-dependent. We obtained boundaries between regular and chaotic regions and found that a larger SOC strength can reduce the size of the chaotic regions. Our findings offer potential applications in precise quantum manipulation and chaos-based quantum technologies. A natural direction is to extend the present analysis to quantum droplets by taking into account the Lee–Huang–Yang (LHY) corrections [45–50].

Acknowledgments

This work was supported by the Project of National Natural Science Foundation of China under Grant No. 12005057, Hunan Provincial Education Office under Grant No. 23B0774, and Innovation and Entrepreneurship Training Program for College Students in Xiangnan University (X2024052).

References

[1] M.H. Anderson, J.R. Ensher, M.R. Matthews, C.E. Wieman, E.A. Cornell, *Science* **269**, 198 (1995).

[2] C.C. Bradley, C.A. Sackett, J.J. Tollett, R.G. Hulet, *Phys. Rev. Lett.* **75**, 1687 (1995).

[3] Y.K. Kato, R.C. Myers, A.C. Gossard, D.D. Awschalom, *Science* **306**, 1910 (2004).

[4] M. König, S. Wiedmann, C. Brüne, A. Roth, H. Buhmann, L.W. Molenkamp, X.L. Qi, S.C. Zhang, *Science* **318**, 766 (2007).

[5] B.A. Bernevig, T.L. Hughes, S.C. Zhang, *Science* **314**, 1757 (2006).

[6] L.J. Lin, K. Jiménez-García, I.B. Spielman, *Nature* **471**, 83 (2011).

[7] Y. Li, L.P. Pitaevskii, S. Stringari, *Phys. Rev. Lett.* **108**, 225301 (2012).

[8] X. Zhou, J. Zhou, C. Wu, *Phys. Rev. A* **84**, 063624 (2011).

[9] Y.V. Kartashov, V.V. Konotop, D.A. Zezyulin, L. Torner, *Phys. Rev. Lett.* **117**, 215301 (2016).

[10] K. Mæland, A.T.G. Janssønn, J.H. Rygh, A. Sudbø, *Phys. Rev. A* **102**, 053318 (2020).

[11] G. Huang, G. Luo, Z. Wu, Z. Xu, *Phys. Rev. A* **103**, 043328 (2021).

[12] X. Luo, Z.Y. Zeng, Y. Guo, B. Yang, J. Xiao, L. Li, C. Kong, A.X. Chen, *Phys. Rev. A* **103**, 043315 (2021).

[13] Y. Luo, X. Wang, L. Luo, Z. Zhou, Z.Y. Zeng, X. Luo, *New J. Phys.* **22**, 093041 (2020).

[14] H. Deng, T. Wan, Y. He et al., *Results Phys.* **31**, 104926 (2021).

[15] Q.B. Wang, J.G. Hu, X.H. Su, L.H. Wen, *Results Phys.* **20**, 103755 (2021).

[16] M.N. Chen, B.J. Liao, H.C. Wang, H. Huang, Y. Liu, D.X. Ling, *Results Phys.* **18**, 103304 (2020).

[17] X.F. Zhang, Y.F. Liu, H.B. Luo, B. Liu, F.Q. Dou, Y. Li, B.A. Malomed, *Phys. Rev. A* **110**, 063302 (2024).

[18] A. Saboo, S. Halder, S. Das, S. Majumder, *Phys. Rev. A* **110**, 033325 (2024).

[19] M. Lepers, V. Zehnlé, J.C. Garreau, *Phys. Rev. Lett.* **101**, 144103 (2008).

[20] J. Martin, B. Georgeot, *Phys. Rev. Lett.* **101**, 074102 (2008).

[21] R.A. Kidd, M.K. Olsen, J.F. Corney, *Phys. Rev. A* **100**, 013625 (2019).

[22] R. Wanzenböck, S. Donsa, H. Hofstätter, O. Koch, P. Schlagheck, I. Březinová, *Phys. Rev. A* **103**, 023336 (2021).

[23] S.C. Li, L. Pezzè, A. Smerzi, *Phys. Rev. A* **103**, 052417 (2021).

[24] W.C. Syu, D.S. Lee, C.Y. Lin, *Phys. Rev. A* **101**, 063622 (2020).

[25] C. Lee, W. Hai, L. Shi, X. Zhu, K. Gao, *Phys. Rev. A* **64**, 053604 (2001).

[26] R. Bürkle, A. Vardi, D. Cohen, J.R. Anglin, *Phys. Rev. Lett.* **123**, 114101 (2019).

[27] A. Dey, D. Cohen, A. Vardi, *Phys. Rev. A* **99**, 033623 (2019).

[28] S. Rong, W. Hai, Q. Xie, Q. Zhu, *Chaos* **19**, 033129 (2009).

[29] Z. Zhou, W. Hai, Y. Deng, Q. Xie, *Chaos Solit. Fract.* **45**, 1423 (2012).

[30] C.J. Liu, Y.C. Meng, J.L. Qin, L. Zhou, *Results Phys.* **43**, 106091 (2022).

[31] J. Larson, B.M. Anderson, A. Altland, *Phys. Rev. A* **87**, 013624 (2013).

[32] C. Kong, H. Chen, C. Li, W. Hai, *Chaos* **28**, 023115 (2018).

[33] C. Kong, X. Luo, H. Chen, Y. Luo, W. Hai, *Chaos* **29**, 103148 (2019).

[34] F.Q. Hu, J.J. Wang, Z.F. Yu, A.X. Zhang, J.K. Xue, *Phys. Rev. E* **93**, 022214 (2016).

[35] L. Salasnich, B.A. Malomed, *Phys. Rev. A* **87**, 063625 (2013).

[36] Y.S. Cheng, G.H. Tang, S.K. Adhikari, *Phys. Rev. A* **89**, 063602 (2014).

[37] A. Smerzi, S. Fantoni, S. Giovanazzi, S.R. Shenoy, *Phys. Rev. Lett.* **79**, 4950 (1997).

[38] W. Hai, C. Lee, G. Chong, L. Shi, *Phys. Rev. E* **66**, 026202 (2002).

[39] X. Luo, W. Hai, *Chaos* **15**, 033702 (2005).

[40] G. Chong, W. Hai, Q. Xie, *Chaos* **14**, 217 (2004).

[41] G. Chong, W. Hai, Q. Xie, *Phys. Rev. E* **71**, 016202 (2005).

[42] W. Hai, S. Rong, Q. Zhu, *Phys. Rev. E* **78**, 066214 (2008).

[43] V.K. Melnikov, *Trans. Moscow Math. Soc.* **12**, 1 (1963).

[44] C. Kong, Y. He, T. Wan, B. Yin, R. Liu, Y. Chen, J. Huang, D. Lei, C. Jiang, H. Deng, *Phys. Lett. A* **458**, 128597 (2023).

[45] H. Kadau, M. Schmitt, M. Wenzel, C. Wink, T. Maier, I. Ferrier-Barbut, T. Pfau, *Nature* **530**, 194 (2016).

[46] I. Ferrier-Barbut, H. Kadau, M. Schmitt, M. Wenzel, T. Pfau, *Phys. Rev. Lett.* **116**, 215301 (2016).

[47] B.A. Malomed, *Front. Phys.* **16**, 22504 (2021).

[48] Z. Luo, W. Pang, B. Liu, Y. Li, B.A. Malomed, *Front. Phys.* **16**, 32201 (2021).

[49] X. Zhang, X. Xu, Y. Zheng, Z. Chen, B. Liu, C. Huang, B.A. Malomed, Y. Li, *Phys. Rev. Lett.* **123**, 133901 (2019).

[50] Y. Li, Z. Luo, Y. Liu, Z. Chen, C. Huang, S. Fu, H. Tan, B.A. Malomed, *New J. Phys.* **19**, 113043 (2017).